Mathematics

https://www.aimspress.com/journal/Math

AIMS Mathematics, 11(8): 27481–27507.
DOI: 10.3934/math.20261100
Received: 25 June 2026
Revised: 15 August 2026
Accepted: 25 August 2026
Published: 31 August 2026

Research article

Analytical bounds and finite element modeling of the temperature distribution on a thin plate heated by a localized radiant source

Jose Lages da Silva Neto[1], **Eduardo D. Correa**[1,2*], **Rogerio M. S. Gama**[1], **and Gustavo R. Anjos**[2]

[1] Department of Mechanical Engineering, Universidade do Estado do Rio de Janeiro–UERJ, Rio de Janeiro, RJ 20550-900, Brazil

[2] Department of Mechanical Engineering/Coppe, Universidade Federal do Rio de Janeiro–UFRJ, Rio de Janeiro, RJ 21941-914, Brazil

* **Correspondence:** Email: eduardo.correa@eng.uerj.br.

Abstract: This work investigates the steady-state temperature field induced on a thin plate by a small high-temperature radiative source placed at a finite distance. A nonlinear source-to-surface model is derived by coupling in-plane heat conduction, a view-factor-based incident radiative flux, and two-sided radiative losses governed by the Stefan–Boltzmann law. The resulting problem is written in weak form and solved with a Newton-linearized finite element formulation. Analytical upper and lower bounds are established for the temperature field, giving admissible limits that are used to assess the numerical results. The implementation is verified with the method of manufactured solutions, for which the relative L^2 and H^1 errors decrease monotonically under mesh refinement. An independent uniform-irradiation benchmark is reproduced to roundoff accuracy, and a separate refinement study for the most localized physical source shows changes below 0.01% between the production and reference meshes. Simulations show a strong dependence on source height: the peak temperature decreases from about 140 to about 22 K as the dimensionless height increases from 0.1 to 10, while the computed extrema remain within the analytical bounds. The rigorous derivation of the radiative source term is restricted to the flat reference plate. Corrugated and perforated geometries are included as illustrative tests of the adaptability of the surface finite element implementation, with corrugated cases interpreted only for very low-amplitude surfaces where self-radiative exchange is neglected.

Keywords: radiative heat transfer; finite element method; Newton linearization; Stefan–Boltzmann law; method of manufactured solutions; a priori bounds
Mathematics Subject Classification: 35J61, 65N30, 80A20

1. Introduction

Radiative heat transfer represents a fundamental physical phenomenon governing energy exchange in high-temperature engineering applications, where thermal radiation often dominates. Practical applications span aerospace thermal control, hypersonic vehicle thermal protection systems, additive manufacturing [1], thermal management of electronic devices, glass manufacturing and ceramics [2], and energy storage systems. Even some devices operating at room temperature can have significant effects of radiation [3].

While classical linear heat conduction problems can be readily solved using established analytical and numerical methods, real-world applications frequently involve the fourth-power temperature dependence via the Stefan-Boltzmann law [4–6]. This nonlinear relationship introduces mathematical complexity, which significantly affects solution behavior, requiring advanced numerical frameworks for accurate prediction [1, 6–8]. Thermal radiation cannot be neglected in such regimes, since the solutions of these problems are strongly affected by nonlinear radiative terms [7, 9].

Thus, the nonlinear mathematical description requires accurate view factor modeling [4, 5, 10], robust boundary condition treatment [11, 12], and numerical methods capable of handling resulting nonlinear equations while maintaining computational efficiency [7, 9, 13, 14].

Several methodological developments have addressed these issues through a variety of approaches. Meshless techniques, including weighted least squares (MWLS) and least-squares methods, have proven effective for nonlinear boundary conditions and temperature-dependent properties [6, 13]. More recently, mesh-free generalized finite difference approaches have been developed for transient heat conduction in functionally graded materials, including spatial–temporal and time-spectral formulations that avoid mesh generation altogether [15, 16]. Finite element frameworks have been extensively developed for conducto-radiative problems in heterogeneous media, with advances in streamline diffusion, contact mechanics, and discrete maximum principle satisfaction [8, 11, 17, 18]. The least-squares finite-element method based on variational principles can be solved efficiently [17].

More recent and advanced approaches include Monte Carlo simulations with discrete ordinate methods [11], neural networks for complex thermal analysis [19], coupled PDE-ODE frameworks for modeling nonlinear transient heat conduction with convective boundary conditions [7], and sophisticated numerical methods for multi-phase and porous media applications [20, 21]. Nonlinear radiative–convective modeling has also been explored in markedly different flow configurations, such as nanofluid flow over rotating disks [22] and magnetized squeezing flow between disks [23], although these studies address boundary-layer nanofluid transport rather than the source-to-surface conducto-radiative problem considered here. Nonlinear heat generation/absorption effects on a heated plane have likewise been analyzed for granular-material flows [24], and comparable nonlinear thermal coupling arises in bioconvective nanofluid transport in physiological settings [25], underscoring that heat-generation nonlinearities of this type are relevant well beyond the specific radiative mechanism treated in this work.

Other numerical strategies for managing radiation nonlinearity include linearization through Kirchhoff transformations for materials with temperature-dependent thermal conductivity [6], iterative coupling schemes [13, 14], and variational principles for nonlinear problems [26]. Recent advances demonstrate successful application of these approaches to problems in porous fins [9, 20, 27], continuous mixtures, and complex material systems [7].

Radiative heat transfer between spatially separated bodies presents unique computational problems addressed through various specialized approaches. Boundary layer studies with convective surface conditions reveal complex radiation-convection interactions [28], while porous media applications, including fins, extended surfaces, and rotating geometries, show significant radiative influence on thermal performance [20, 21, 29–31].

From a modeling standpoint, two ingredients are central: (i) the Stefan–Boltzmann nonlinearity and (ii) the geometric coupling encoded by radiation view factors. Classical radiative-transfer references and general view-factor reviews show that the radiative exchange term is essentially geometric and can be strongly affected by source-target distance, relative orientation, and surface shape [4, 5, 10]. These features make the resulting temperature field naturally dependent on both the nonlinear thermal law and the spatial structure of the radiative kernel.

This observation motivates the treatment of radiative exchange as a nonlinear source term within a PDE framework, rather than as a purely empirical thermal correction. In this setting, the spatially varying radiation kernel acts as a geometric forcing mechanism that must be coupled consistently with in-plane heat conduction.

However, significant gaps remain in strongly coupled conducto-radiative scenarios involving distant source-target configurations with complex view factor relationships. Irradiation non-uniformity translates directly into pronounced temperature non-uniformity and performance penalties, underscoring the need for models that resolve both the radiative forcing and the in-plane conductive response.

The mathematical formulation developed in this work leads to a two-dimensional nonlinear partial differential equation with homogeneous Neumann boundary conditions. The problem is treated through a weak variational formulation combined with Newton's method, which allows the nonlinear radiative term to be handled in a systematic and computationally efficient manner. This strategy is consistent with established variational and numerical approaches for nonlinear thermal problems and PDEs posed on complex geometries [3, 11, 17, 32–34], while being specifically adapted here to a distant source–target radiative configuration. More broadly, the emphasis on model derivation, qualitative consistency, and numerical simulation follows the mathematical-modeling perspective adopted in transport-type applied PDE problems.

Unlike previous studies that treat radiative boundary conditions empirically or restrict the geometric coupling to simplified view factors, the present work derives the source-to-surface radiative term directly from the source-plate geometry and couples it consistently with in-plane conduction within a single nonlinear PDE framework. The main contributions of this study are threefold: first, the derivation of a mathematically consistent nonlinear source-to-surface model, together with explicit analytical upper and lower bounds for the temperature field; second, a finite element procedure based on Newton linearization of the weak form, written on the surface through the Laplace–Beltrami operator so that the same implementation can be applied to flat and non-flat meshes; and third, the verification of the implementation through the method of manufactured solutions, together with a quantitative analysis of how the source height controls the temperature distribution.

The methodology is relevant to engineering situations involving localized radiant heating, such as infrared-lamp or radiant-panel heating of plates and moving webs, radiant testing of surfaces, and components placed near concentrated high-temperature sources. A flat rectangular plate is adopted as the reference configuration; the corrugated and perforated examples are included as demonstrations of the surface finite element implementation rather than as a rigorous derivation of radiative exchange on general curved surfaces.

2. Mathematical model

The proposed model applies to opaque surfaces for which the incident radiation from the source is assumed to be absorbed, with reflection neglected; Figure 1 shows representative examples of such surfaces. The precise meaning of this assumption, and its relation to the gray-surface hypothesis adopted in the heat balance, is discussed below.

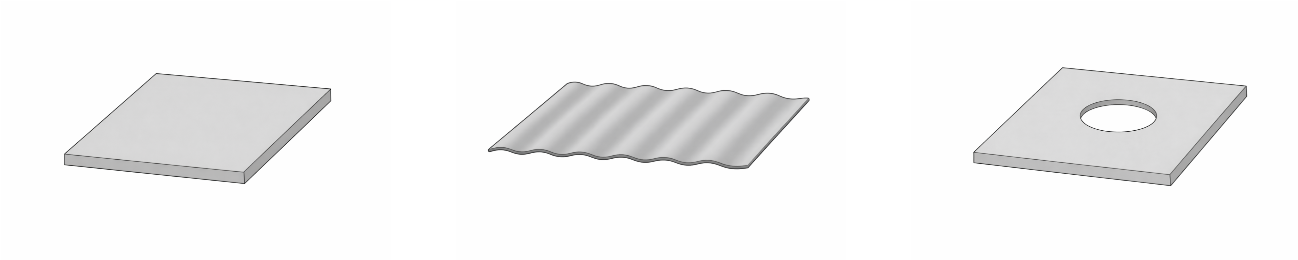

(a) Flat surface **(b)** Corrugated surface **(c)** Flat surface with hole

Figure 1. Surfaces.

To develop our model, we consider two idealized surfaces: a small thermal radiant source, represented by a thin flat disk, and the receiving body, a planar rectangular plate of very small thickness. A scheme of the studied problem is illustrated in Figure 2. The thermal radiant source will be represented by a (very) small disk (assumed to be a blackbody), at a constant temperature T_S, represented by the bounded open set

$$\Gamma \equiv \{(u, v, w) \text{ such that } (u - \bar{a})^2 + (v - \bar{b})^2 < R^2,\ H < w < H + \delta,\ \delta \to 0\}, \tag{2.1}$$

where $R \ll H$ is assumed for the small-disk (point-source) approximation used throughout; the associated approximation error is quantified in Section 5. A part of the thermal radiant energy emerging from the disk will reach the plane z = constant.

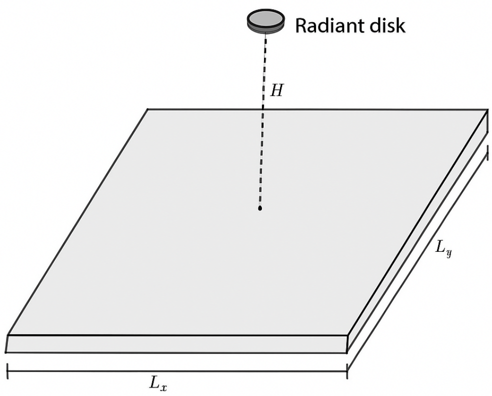

Figure 2. A scheme of the considered problem.

Denoting by P a point on the lower surface of the small disk (thermal radiant source) and by Q a point on the plane z = constant, we have that

$$\begin{aligned} \mathbf{P} &= (u\,\mathbf{i} + v\,\mathbf{j} + H\,\mathbf{k}) && \rightarrow \text{a point on the lower surface of the small disk (source),} \\ \mathbf{Q} &= (x\,\mathbf{i} + y\,\mathbf{j} + z_0\,\mathbf{k}) && \rightarrow \text{a point on the plane } z = z_0 = \text{constant,} \\ \mathbf{P} - \mathbf{Q} &= (u - x)\,\mathbf{i} + (v - y)\,\mathbf{j} + (H - z_0)\,\mathbf{k}. \end{aligned} \tag{2.2}$$

So, the kernel associated to the view factor between the source and the plane is given by

$$\begin{aligned} K(\mathbf{P}, \mathbf{Q}) &= \frac{((u-x)\mathbf{i} + (v-y)\mathbf{j} + (H-z_0)\mathbf{k})\cdot\mathbf{k}\ ((u-x)\mathbf{i} + (v-y)\mathbf{j} + (H-z_0)\mathbf{k})\cdot\mathbf{k}}{\pi((u-x)^2 + (v-y)^2 + (H-z_0)^2)^2} \\ &= \frac{(H-z_0)^2}{\pi((u-x)^2 + (v-y)^2 + (H-z_0)^2)^2}. \end{aligned} \tag{2.3}$$

Equivalently, writing $r = \|\mathbf{P} - \mathbf{Q}\|$ and $\cos\theta_P = \cos\theta_Q = (H - z_0)/r$ for the unit outward normals of the horizontal source and receiving surfaces, the kernel takes the standard radiometric form $K(\mathbf{P}, \mathbf{Q}) = \cos\theta_P \cos\theta_Q/(\pi r^2)$, consistent with the vector-notation derivation above [4, 5].

In this way, the thermal radiant energy, per unit time and per unit area, incident on the plane (coming from the source), at a given point (x, y, z) is given by

$$e_{\text{SOURCE}} = \int_{SOURCE} \sigma\, T_S^4\ K(\mathbf{P}, \mathbf{Q})\ du\, dv, \tag{2.4}$$

(σ: Stefan-Boltzmann constant).

Since the source is assumed to be a small disk (with radius R) centered at $(x, y) = (\bar{a}, \bar{b})$, the above integral may be approximated by

$$e_{\text{SOURCE}} = \frac{\sigma\, T_S^4\, (H - z_0)^2\, \pi\, R^2}{\pi((\bar{a} - x)^2 + (\bar{b} - y)^2 + (H - z_0)^2)^2}. \tag{2.5}$$

The quantity e_{SOURCE} represents the amount of thermal radiant energy that, emerging from the source, reaches the point (x, y, z_0) on the plane. It should be noted that only the energy emitted from the lower surface of the disk reaches the plane.

Hence, let us define the horizontal flat plate as the following bounded open set, illustrated in Figure 3.

$$\Omega \ \equiv\ \{(x, y, z) \in \mathbb{R}^3 \mid 0 < x < L_X,\ 0 < y < L_Y,\ -\delta < z < \delta,\ \delta \rightarrow 0\}. \tag{2.6}$$

Here, δ denotes the plate half-thickness, so that the total physical thickness is $t = 2\delta$.

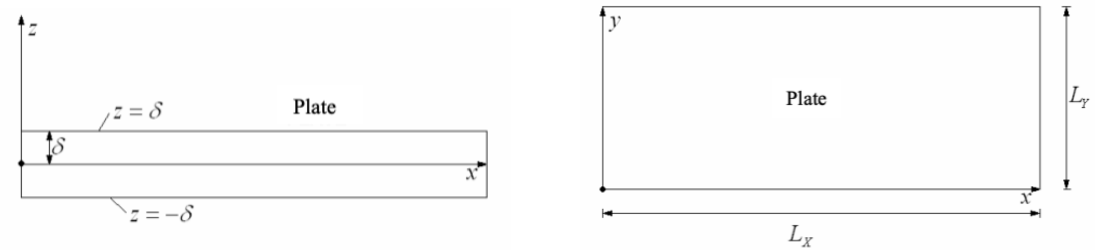

(a) View - plane xz **(b)** View - plane xy

Figure 3. The considered flat plate (two views).

There exists a thermal radiant emission from the source to the plate. A part of the emitted thermal radiation from the subset of the boundary in which $w = H$ will reach the plate on its upper side.

Now, denoting by $\mathbf{P}$ a point on the lower surface of the small disk (thermal radiant source) and by $\mathbf{Q}$ a point on the upper surface of the horizontal plate, we have that

$$\begin{aligned} \mathbf{P} &= (u\,\mathbf{i} + v\,\mathbf{j} + H\,\mathbf{k}), \\ \mathbf{Q} &= (x\,\mathbf{i} + y\,\mathbf{j} + \delta\,\mathbf{k}), \\ \mathbf{P} - \mathbf{Q} &= (u - x)\,\mathbf{i} + (v - y)\,\mathbf{j} + (H - \delta)\,\mathbf{k}. \end{aligned} \tag{2.7}$$

So, the kernel associated to the view factor between the lower surface of the source and the upper surface of the plate is given by (taking into account that $\delta \to 0$):

$$K(\mathbf{P}, \mathbf{Q}) = \frac{H^2}{\pi\big((u - x)^2 + (v - y)^2 + H^2\big)^2}. \tag{2.8}$$

In this way, the thermal radiant energy, per unit time and per unit area, incident on the plate (coming from the source), at a given point (x, y, δ), is given by

$$e_{\mathrm{SOURCE}}(x, y, \delta) = \iint_\Gamma \frac{\sigma\, T_S^4\, H^2}{\pi\big((u - x)^2 + (v - y)^2 + H^2\big)^2}\, dA. \tag{2.9}$$

Since the source is assumed to be a small disk (with radius R) centered at $(x, y) = (\bar{a}, \bar{b})$, the above integral may be approximated by

$$e_{\mathrm{SOURCE}} = \frac{\sigma\, T_S^4\, H^2\, \pi\, R^2}{\pi\big((\bar{a} - x)^2 + (\bar{b} - y)^2 + H^2\big)^2}. \tag{2.10}$$

The quantity e_{SOURCE} represents the amount of thermal radiant energy that, emerging from the source, reaches the point (x, y, δ) on the plate (upper surface).

It should be noted that there exists a thermal radiant loss from the plate to the environment (from both sides of the plate).

The plate is assumed to be opaque, gray, and at rest. For an opaque surface, the absorptivity, reflectivity, and emissivity satisfy $\alpha + \rho = 1$, and, by Kirchhoff's law for a gray surface, $\alpha = \varepsilon$, so that $\rho = 1 - \varepsilon$. The idealization of negligible reflection of the incident source flux therefore corresponds to a strongly absorbing surface ($\alpha \to 1$); it is representative of many engineering surfaces of practical interest, such as oxidized metals, coated or roughened surfaces, and high-temperature ceramics, and it yields a conservative upper estimate of the absorbed energy, since any reflected fraction would reduce the net flux deposited on the plate. Accordingly, the radiation emitted by the source is taken to be partially absorbed by the plate, whereas the plate emits its own thermal radiation as a gray body of emissivity ε; a partially reflecting surface can be accommodated by multiplying the incident source term by the absorptivity α. Since the plate is thin and at rest, the heat transfer process within it takes place by conduction. Assuming steady-state heat transfer, the energy transfer process in the plate (with no internal heat sources) is described by the following partial differential equation:

$$\frac{\partial}{\partial x}\Big(k\,\frac{\partial T}{\partial x}\Big) + \frac{\partial}{\partial y}\Big(k\,\frac{\partial T}{\partial y}\Big) + \frac{\partial}{\partial z}\Big(k\,\frac{\partial T}{\partial z}\Big) = 0 \quad \text{in } \Omega, \tag{2.11}$$

in which k denotes the thermal conductivity, assumed here a constant.

Since the plate is assumed to be thin, the area of the lateral edges $x = 0$, $x = L_X$, $y = 0$, and $y = L_Y$ is negligible compared with the area of the two large faces; as a modeling assumption, valid when the convective coefficient and the temperature difference at the edges remain moderate, the heat exchanged through the edges is therefore treated as insignificant relative to that exchanged with the source and the environment over the faces. For the small-to-moderate source heights considered in most of this work ($H \leq 1$), the source is centered over the plate and the radiative forcing decays rapidly away from its projection, so the flux reaching the lateral edges is vanishingly small; for the largest height studied ($H = 10$) the incident field becomes broad rather than strongly localized, and the near-uniform temperature field observed in that case follows instead from the combination of this broad forcing and efficient in-plane conduction (Section 5). It is therefore reasonable to model these edges as adiabatic, or thermally insulated, which leads to the homogeneous Neumann boundary conditions adopted below. This is also the natural boundary condition of the weak formulation, requiring no additional boundary data.

Define the mean temperature $\overline{T}$ (that is a function of x and y) as follows:

$$\overline{T}(x, y) = \frac{1}{2\delta} \int_{-\delta}^{\delta} \widehat{T}(x, y, z)\, dz, \qquad T = \widehat{T}(x, y, z). \tag{2.12}$$

From this point onward, $\overline{T}$ (or, where the overbar is omitted for brevity, T without a hat) always denotes the through-thickness mean/averaged temperature; $\widehat{T}$ denotes the pointwise three-dimensional field, used only where the through-thickness variation is explicit, as in the definition above. Taking into account that $\delta \to 0$, equation (2.11) may then be integrated over the thickness 2δ, giving rise to

$$\frac{\partial}{\partial x}\Big(k \frac{\partial T}{\partial x}\Big) + \frac{\partial}{\partial y}\Big(k \frac{\partial T}{\partial y}\Big) + \frac{1}{2\delta}\Big[k \frac{\partial T}{\partial z}\Big]_{z=\delta} - \frac{1}{2\delta}\Big[k \frac{\partial T}{\partial z}\Big]_{z=-\delta} = 0. \tag{2.13}$$

Taking into account the thermal radiation heat transfer to the plate yields

$$\begin{aligned} (-\, k\, \tfrac{\partial T}{\partial z})_{z=\delta} &= \text{energy transfer (per unit time and per unit area) leaving the surface } z = \delta, \\ (k\, \tfrac{\partial T}{\partial z})_{z=-\delta} &= \text{energy transfer (per unit time and per unit area) leaving the surface } z = -\delta. \end{aligned} \tag{2.14}$$

Equation (2.13) will be subjected to the following Neumann boundary conditions (insulated subsets):

$$\frac{\partial \overline{T}}{\partial x} = 0, \quad x = 0 \text{ and } x = L_X, \qquad \frac{\partial \overline{T}}{\partial y} = 0, \quad y = 0 \text{ and } y = L_Y. \tag{2.15}$$

Taking into account the source and the thermal radiant energy emitted from the surface $z = \delta$, and making the nonlinear term $\overline{T}^4 = |\overline{T}|^3 \cdot \overline{T}$ [9], we have

$$(-\, k\, \tfrac{\partial T}{\partial z})_{z=\delta} = \varepsilon\, \sigma\, |\overline{T}|^3\, \overline{T} \;-\; \frac{\sigma\, \overline{T}_S^4\, H^2\, R^2}{\left((\bar{a} - x)^2 + (\bar{b} - y)^2 + H^2\right)^2} \tag{2.16}$$

(ε: emissivity of the plate).

On the other hand, since the source does not emit thermal radiant energy for the surface $z = -\delta$, we have

$$(k\, \tfrac{\partial T}{\partial z})_{z=-\delta} = \varepsilon\, \sigma\, |\overline{T}|^3\, \overline{T}. \tag{2.17}$$

Therefore, Equation (2.13) can be rewritten as

$$\frac{\partial}{\partial x}\Big(k\,\frac{\partial \overline{T}}{\partial x}\Big)+\frac{\partial}{\partial y}\Big(k\,\frac{\partial \overline{T}}{\partial y}\Big)-\frac{1}{2\delta}\Big[\,\varepsilon\,\sigma\,|\overline{T}|^{3}\,\overline{T}\;-\;\frac{\sigma\,\overline{T}_{S}^{4}\,H^{2}\,R^{2}}{\big((\bar{a}-x)^{2}+(\bar{b}-y)^{2}+H^{2}\big)^{2}}\Big]-\frac{1}{2\delta}(\varepsilon\,\sigma\,|\overline{T}|^{3}\,\overline{T})=0. \quad (2.18)$$

For the considered steady-state phenomenon, the complete mathematical description becomes

$$\frac{\partial}{\partial x}\Big(k\,\frac{\partial \overline{T}}{\partial x}\Big)+\frac{\partial}{\partial y}\Big(k\,\frac{\partial \overline{T}}{\partial y}\Big)-\frac{\varepsilon\,\sigma}{\delta}\,|\overline{T}|^{3}\,\overline{T}+\frac{\sigma\,\overline{T}_{S}^{4}\,H^{2}\,R^{2}}{2\,\delta\Big((\bar{a}-x)^{2}+(\bar{b}-y)^{2}+H^{2}\Big)^{2}}=0. \quad (2.19)$$

and is inherently nonlinear.

Assuming constant thermal conductivity, we may rewrite the problem as follows:

$$\frac{\partial^{2}\overline{T}}{\partial x^{2}}+\frac{\partial^{2}\overline{T}}{\partial y^{2}}-A\,|\overline{T}|^{3}\,\overline{T}+\frac{B}{\Big((\bar{a}-x)^{2}+(\bar{b}-y)^{2}+H^{2}\Big)^{2}}=0, \quad (2.20)$$

in which the constants A and B are given by

$$A=\frac{\varepsilon\,\sigma}{\delta\,k}, \qquad B=\frac{\sigma\,\overline{T}_{S}^{4}\,H^{2}\,R^{2}}{2\,\delta\,k}. \quad (2.21)$$

With $[\sigma] = \mathrm{W\,m^{-2}K^{-4}}$, $[\delta] = \mathrm{m}$, and $[k] = \mathrm{W\,m^{-1}K^{-1}}$, dimensional analysis gives $[A] = \mathrm{m^{-2}K^{-3}}$ and $[B] = \mathrm{m^{2}K}$, so that both $A|\overline{T}|^{3}\overline{T}$ and $B/[(\bar{a}-x)^{2}+(\bar{b}-y)^{2}+H^{2}]^{2}$ carry units of $\mathrm{K\,m^{-2}}$, consistent with $\nabla^{2}\overline{T}$ in Eq (2.20).

At this point, it is possible (and convenient) to establish an "a priori" upper bound for the solution. To establish this bound, let us take into account that $\overline{T}$ assumes its maximum in a neighborhood Δ in which

$$\int_{\partial\Delta}\nabla\overline{T}\cdot\mathbf{n}\,dA\leq 0. \quad (2.22)$$

So, in this neighborhood, we must have

$$A\,|\overline{T}|^{3}\,\overline{T}\leq\frac{B}{\Big((\bar{a}-x)^{2}+(\bar{b}-y)^{2}+H^{2}\Big)^{2}}. \quad (2.23)$$

and, therefore (upper bound for $\overline{T}$),

$$\overline{T}\;\leq\;\sup_{\Omega}\left\{\frac{\frac{B}{A}}{\big((\bar{a}-x)^{2}+(\bar{b}-y)^{2}+H^{2}\big)^{2}}\right\}^{1/4}\;\leq\;\frac{1}{H}\Big(\frac{B}{A}\Big)^{1/4}. \quad (2.24)$$

On the other hand, assuming that $\overline{T}$ assumes its minimum in a neighborhood Δ, we have

$$\int_{\partial\Delta}\nabla\overline{T}\cdot\mathbf{n}\,dA\;\geq\;0. \quad (2.25)$$

So, in this neighborhood, we must have

$$A\,|\overline{T}|^{3}\,\overline{T}\;\geq\;\frac{B}{\big((\bar{a}-x)^{2}+(\bar{b}-y)^{2}+H^{2}\big)^{2}}. \quad (2.26)$$

and, therefore (lower bound for $\overline{T}$),

$$\overline{T} \;\geq\; \inf_{\Omega}\left\{\frac{\frac{B}{A}}{\left((\bar{a}-x)^2+(\bar{b}-y)^2+H^2\right)^2}\right\}^{1/4} \;=\; \left\{\frac{\frac{B}{A}}{\left(\sup_{\Omega}(\bar{a}-x)^2+\sup_{\Omega}(\bar{b}-y)^2+H^2\right)^2}\right\}^{1/4}. \tag{2.27}$$

Hence, for cases in which $0 \leq \bar{a} \leq L_X$ and $0 \leq \bar{b} \leq L_Y$, the following holds (lower bound for $\overline{T}$):

$$\overline{T} \;\geq\; \left\{\frac{\frac{B}{A}}{\left(L_X^2+L_Y^2+H^2\right)^2}\right\}^{1/4}. \tag{2.28}$$

These bounds also shed light on the well-posedness of the problem. Writing the steady-state balance in weak form, the associated operator is the sum of the linear elliptic Laplacian term and the nonlinear reaction term $A\,|\overline{T}|^3\,\overline{T}$. The latter is monotone increasing in $\overline{T}$, since the map $s \mapsto A\,|s|^3 s$ has non-negative derivative $4A\,|s|^3 \geq 0$. Added to the monotone and coercive Laplacian, it yields a strictly monotone, coercive, and continuous operator on $H^1(\Omega)$, using the continuous embedding $H^1(\Omega) \hookrightarrow L^p(\Omega)$ for every finite p on the bounded, Lipschitz, two-dimensional domain Ω [35]. By the theory of monotone operators, in the sense of Browder–Minty, the corresponding nonlinear variational problem admits a unique weak solution, and the a priori upper and lower bounds derived above guarantee that this solution is bounded and physically admissible. This monotonicity supports the well-posedness of the continuous problem and is consistent with the stable behavior observed in the Newton iterations.

3. Numerical analysis

Consider the standard Sobolev spaces: $L^2(\Omega)$, the space of square-integrable functions on Ω, and $H^1(\Omega)$, the space of functions in $L^2(\Omega)$ whose first derivatives are also in $L^2(\Omega)$. We define the trial and test spaces depending on the boundary conditions: $V = H^1(\Omega)$, for homogeneous Neumann boundary condition, and $V = \{v \in H^1(\Omega) \mid v = 0 \text{ on } \Gamma_D\}$, for Dirichlet boundary condition on $\Gamma_D \subset \partial\Omega$. The Dirichlet space is introduced because it is used later for the method of manufactured solutions verification (Section 3.2), where exact Dirichlet data are imposed on the entire boundary; the physical simulations reported in this work use only the homogeneous Neumann space.

We consider the steady-state heat conduction problem with radiative emission and a radiative source governed by Eq (2.19); for constant thermal conductivity this reduces to Eq (2.20). The surface finite element extension to non-flat meshes is obtained through the Laplace–Beltrami operator, as described below.

We must find $T \in V$ such that for all $v \in V$:

$$\int_{\Omega} k\nabla T \cdot \nabla v\, d\Omega + \int_{\Omega} kA|T|^3 T v\, d\Omega = \int_{\Omega} k f v\, d\Omega, \qquad f(x,y) = \frac{B}{((\bar{a}-x)^2+(\bar{b}-y)^2+H^2)^2}, \tag{3.1}$$

where homogeneous Neumann boundary conditions have been imposed, so that the boundary term $\oint_{\partial\Omega} v(k\nabla T)\cdot \mathbf{n}\, dS$ vanishes identically; this is the conventional weak form of the governing equation, Eq (2.20).

The boundary conditions represent the physical constraints at the plate edges. For the specific case analyzed, the plate is assumed to have insulated edges with no heat loss across the boundaries, leading to homogeneous Neumann conditions, $\nabla T \cdot \mathbf{n} = 0 \quad \text{on } \Gamma_{N1} \subset \partial\Omega$.

3.1. Definition of the matrices

The matrices defined below are central to the finite element discretization of the radiative heat transfer problem on a two-dimensional surface embedded in $\mathbb{R}^3$ (e.g., a thin plate with spatially varying temperature). The first matrix, $\mathbf{K_s}$, represents the generalized stiffness matrix associated with thermal conduction, where the thermal conductivity k is assumed to be piecewise constant over each finite element. It is formed by integrating the dot product of the spatial gradients of the shape functions over the domain Ω. The operator ∇_s denotes the surface gradient operator, i.e., the tangential gradient defined on the shell midsurface: $\nabla_s v = (\mathbf{I} - \mathbf{n} \otimes \mathbf{n})\nabla\tilde{v}$, where $\mathbf{n}$ is the unit normal to the surface and $\tilde{v}$ is any smooth extension of v off the surface. The second matrix, $\mathbf{M_{rad_s}}$, is the nonlinear radiation Jacobian. Its temperature-dependent factor is evaluated from the finite element temperature interpolated at each quadrature point. The integral combines this temperature weighting with the product of shape functions, scaled by the emissivity ε, the Stefan-Boltzmann constant σ, and the plate thickness δ. The third matrix, $\mathbf{M_s}$, is the standard finite element mass matrix, capturing the projection of source terms onto the finite element space through the shape function products $N_i N_j$. Together, these matrices enable the construction of the linearized system solved at each Newton iteration.

- Stiffness matrix (considering k constant element-wise):

$$\mathbf{K_s} = \int_\Omega \nabla_s N_i \cdot \nabla_s N_j \, d\Omega. \tag{3.2}$$

- Temperature-weighted mass matrix evaluated with quadrature-point temperatures:

$$\mathbf{M_{rad_s}} = \int_\Omega 4A \left|T^{(n)}\right|^3 N_i N_j \, d\Omega. \tag{3.3}$$

  Here, $T^{(n)}$ denotes the finite element temperature interpolated from the eight Quad8 nodal values at each quadrature point. The factor $4A|T^{(n)}|^3$ is therefore evaluated pointwise and integrated together with $N_i N_j$ and the surface Jacobian using the 3×3 Gauss rule. The nonlinear radiative residual and its Newton Jacobian are assembled consistently with this same quadrature-point temperature, without an element-average approximation.

- Standard mass matrix :

$$\mathbf{M_s} = \int_\Omega N_i N_j \, d\Omega \tag{3.4}$$

Each surface element is first expressed in a local orthonormal plane. The first local direction follows the corner edge $v_1 \to v_2$, and the second is obtained by removing from $v_1 \to v_3$ its component along the first direction. The eight three-dimensional nodal coordinates are projected onto this local basis. The mapping from the reference square to the resulting two-dimensional element is isoparametric: the same eight quadratic shape functions interpolate the geometry and the temperature. The Jacobian and the transformed shape-function gradients are evaluated separately at every quadrature point. The stiffness, standard mass, and radiation-weighted contributions are integrated with the tensor-product 3×3 Gauss rule, i.e., nine quadrature points per element.

The adopted approximation is the eight-node quadratic serendipity quadrilateral, commonly denoted Quad8 and illustrated in Figure 4; it is not the complete nine-node biquadratic quadrilateral.

Four nodes are located at the corners and four at the edge midsides. Their positions define the isoparametric geometry, so a displaced midside node can represent a curved quadratic edge. In the meshes reported in this work, however, the in-plane domain is rectangular and its boundary edges are straight; non-flat surface geometry is treated element by element through the local-plane construction described above.

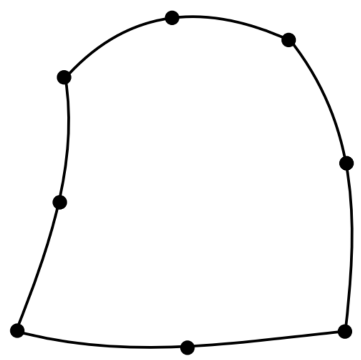

Figure 4. Topology of the eight-node quadratic serendipity quadrilateral (Quad8). Corner and midside nodes define the isoparametric mapping and can represent quadratic edges; the reported rectangular meshes use straight boundary edges.

3.2. Manufactured solution

The method of manufactured solutions (MMS) is employed to verify the correctness and convergence properties of the numerical formulation. In this approach, an analytical temperature field $T(x, y)$ is prescribed, and the corresponding source term $Q(x, y)$ is constructed such that the chosen solution satisfies the governing differential equation.

The strong form of the problem is given by:

$$\nabla \cdot (\nabla T) - A\,|T|^3 T + \frac{B}{\left[(\bar{a} - x)^2 + (\bar{b} - y)^2 + H^2\right]^2} + Q(x, y) = 0. \tag{3.5}$$

In contrast to simpler trigonometric fields, a higher-order manufactured solution is adopted in order to better excite the numerical discretization and assess convergence more rigorously. The analytical solution is defined as:

$$T(x, y) = 1 + \sin(2\pi x)\sin(3\pi y) + 0.5\cos(5\pi x)\cos(4\pi y) + 0.2\,x^2y^2. \tag{3.6}$$

The MMS verification is performed on the flat reference surface, with $z = 0$; no corrugation is applied to this test. The boundary conditions used in the MMS verification differ from those of the physical problem. The homogeneous Neumann conditions stated above are retained for the physical simulations, whereas the MMS computations impose the exact Dirichlet data obtained from Eq (3.6) on the entire boundary, $T_h = T$ on $\partial\Omega$. Consequently, at every Newton iteration the boundary temperature is set to the manufactured value, and the corresponding temperature increment satisfies $\Delta T = 0$ at all boundary nodes.

This choice introduces multiple spatial scales and polynomial components, ensuring that both the interpolation capabilities of the finite element basis and the nonlinear terms of the governing equation are thoroughly tested.

By substituting Eq (3.6) into Eq (3.5), the source term $Q(x, y)$ is obtained as:

$$Q(x,y) = -\nabla \cdot (\nabla T) + A\,|T|^3 T - \frac{B}{\left[(\bar{a}-x)^2 + (\bar{b}-y)^2 + H^2\right]^2} \tag{3.7}$$

where the Laplacian of the manufactured solution is computed analytically.

The first term on the right-hand side corresponds to **thermal conduction**, represented by the Laplacian operator $k\nabla^2 T$. The second term accounts for the **nonlinear radiative emission**, which follows a reduced Stefan–Boltzmann law proportional to $|T|^3 T$. The third term represents the **external radiative source**, corresponding to energy incoming from a localized source positioned above the plate. Finally, the term $Q(x, y)$ acts as a compensating forcing term that ensures that the manufactured solution exactly satisfies the governing equation.

Once the source term is defined, the numerical problem is solved using the weak form with $Q(x, y)$ included. The resulting numerical solution must converge to the analytical field $T(x, y)$.

The nonlinear iterations are monitored over the set $\mathcal{F}$ of free temperature degrees of freedom. The vector on the right-hand side of the linearized system is the negative discrete nonlinear residual at the current iterate.

At each Newton iteration n, the linearized weak form leads to the following matrix system and updated T^{n+1}:

$$(\mathbf{K_s} + \mathbf{M_{rad_s}})\Delta T^{(n+1)} = -\left(\mathbf{K_s} + \frac{\mathbf{M_{rad_s}}}{4}\right)T^{(n)} + \mathbf{M_s}\left[\frac{B}{[(a-x_i)^2 + (b-y_i)^2 + H^2]^2}\right], \tag{3.8}$$

$$T^{(n+1)} = T^{(n)} + \Delta T. \tag{3.9}$$

The relative increment and residual indicators are defined as

$$\eta_T^{(n+1)} = \frac{\|\Delta T_{\mathcal{F}}^{(n+1)}\|_2}{\max\left(1, \|T_{\mathcal{F}}^{(n+1)}\|_2\right)}, \qquad \eta_R^{(n)} = \frac{\|\mathbf{R}_{\mathcal{F}}^{(n)}\|_2}{\max\left(1, \|\mathbf{R}_{\mathcal{F}}^{(0)}\|_2\right)}.$$

Convergence is accepted only when both $\eta_T^{(n+1)} < 10^{-6}$ and $\eta_R^{(n)} < 10^{-6}$. The Newton updates are applied without damping or a line search.

The iterative process continues until convergence is achieved. Due to the construction of the source term, the numerical solution is expected to recover the manufactured solution up to discretization errors. This provides a rigorous framework for verifying both the implementation and the expected convergence rates of the numerical method.

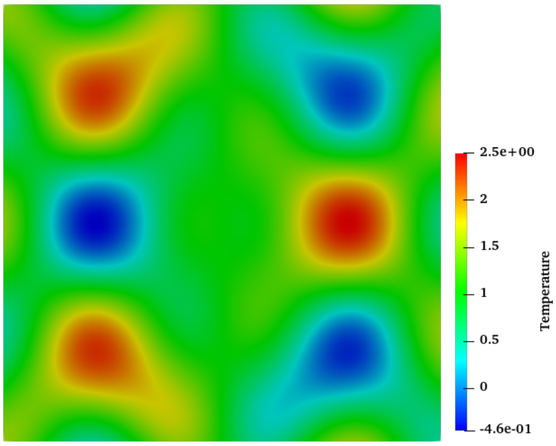

Figure 5. Numerical solution obtained using the manufactured source term. The computed temperature field accurately reproduces the prescribed analytical solution, verifying the numerical implementation.

4. Error norms and convergence analysis

In order to assess the accuracy and convergence properties of the numerical solution, two standard norms are employed: the L^2 norm and the H^1 norm [35]. These norms provide complementary information about the quality of the approximation obtained by the finite element method.

Let T denote the exact (analytical or manufactured) solution and T_h the finite element approximation. The error is defined as:

$$e = T_h - T. \tag{4.1}$$

4.1. Relative L^2 error norm

The L^2 norm measures the average error over the computational domain Ω, and is defined as:

$$||e||_{L^2} = \left(\int_\Omega (T_h - T)^2 \, d\Omega \right)^{1/2}. \tag{4.2}$$

In order to obtain a scale-independent metric, the relative L^2 error is used:

$$||e||_{L^2}^{rel} = \left(\frac{\int_\Omega (T_h - T)^2 \, d\Omega}{\int_\Omega T^2 \, d\Omega} \right)^{1/2}. \tag{4.3}$$

In this MMS verification section, $\mathbf{M}$ and $\mathbf{K}$ denote the standard mass and stiffness matrices associated with the two-dimensional reference discretization; the subscript s is reserved for the surface matrices used in the general surface formulation. Within the finite element framework, this quantity is computed using the consistent mass matrix $\mathbf{M}$:

$$||e||_{L^2}^{rel} = \left(\frac{\mathbf{e}^T \mathbf{M} \mathbf{e}}{\mathbf{T}^T \mathbf{M} \mathbf{T}} \right)^{1/2}. \tag{4.4}$$

For the MMS verification, the integrals in the relative norms are evaluated element by element using the same 3×3 Gauss rule employed in the finite element assembly. At every quadrature point, the numerical field and its gradient are reconstructed as $T_h = \sum_i N_i T_i$ and $\nabla T_h = \sum_i \nabla N_i T_i$, while the exact manufactured field T and its analytical gradient are evaluated at the same physical coordinates. Consequently, the computed quantity is the error $T_h - T$ throughout each element, rather than the difference between the numerical nodal vector and the nodal interpolant of the exact solution.

The L^2 norm quantifies the global (mean-square) accuracy of the solution and is particularly useful for assessing convergence rates.

4.2. Relative H^1 error norm

The H^1 norm extends the L^2 norm by incorporating the gradient. It is defined as:

$$\|e\|_{H^1} = \left(\int_\Omega (T_h - T)^2 \, d\Omega + \int_\Omega \|\nabla T_h - \nabla T\|^2 \, d\Omega \right)^{1/2}. \tag{4.5}$$

The corresponding relative H^1 error is given by:

$$\|e\|_{H^1}^{rel} = \left(\frac{\int_\Omega (T_h - T)^2 \, d\Omega + \int_\Omega \|\nabla T_h - \nabla T\|^2 \, d\Omega}{\int_\Omega T^2 \, d\Omega + \int_\Omega \|\nabla T\|^2 \, d\Omega} \right)^{1/2}. \tag{4.6}$$

In discrete form, this norm can be computed using both the mass matrix $\mathbf{M}$ and the stiffness matrix $\mathbf{K}$:

$$\|e\|_{H^1}^{rel} = \left(\frac{\mathbf{e}^T\mathbf{M}\mathbf{e} + \mathbf{e}^T\mathbf{K}\mathbf{e}}{\mathbf{T}^T\mathbf{M}\mathbf{T} + \mathbf{T}^T\mathbf{K}\mathbf{T}} \right)^{1/2}. \tag{4.7}$$

The H^1 norm is particularly relevant for diffusion-dominated problems, as it directly measures the error in both the solution and its gradient. Since the governing equation involves the Laplacian operator, which depends on spatial derivatives, the H^1 norm provides a more physically meaningful measure of accuracy, especially in terms of heat flux prediction.

The flat-plate MMS study uses $A = 5.103 \times 10^{-6}$, $B = 1.161216$, $H = 0.1$, and $a = b = 0.5$ on the unit square. The nominal boundary-refinement sequence is 2, 4, 10, 20, and 100; the corresponding unstructured Quad8 meshes and their actual maximum element sizes are reported in Table 1. The nonlinear system is assembled with the 3×3 Gauss rule and initialized with $T_h^{(0)} = 300$. Exact Dirichlet data from Eq (3.6) are imposed on the entire boundary. Newton iteration is stopped only when both the relative increment and the initial-residual-normalized nonlinear residual over the free degrees of freedom are below 10^{-6}. Neither damping nor a line search is used. All five cases converge in eight Newton updates.

Because the successive unstructured meshes do not provide exact halvings of h, the observed orders in Table 1 are calculated with the actual mesh-size ratio, $p = \log(E_{h_{i-1}}/E_{h_i})/\log(h_{i-1}/h_i)$.

Table 1. Flat-plate MMS convergence data obtained with Quad8 elements and the 3×3 Gauss rule. N_{dof} denotes the total number of temperature degrees of freedom, including those constrained by the exact Dirichlet boundary data.

N_{el}	N_{dof}	h	$\lVert e\rVert_{L^2}^{rel}$	p_{L^2}	$\lVert e\rVert_{H^1}^{rel}$	p_{H^1}	N_{Newton}
4	21	5.0000×10^{-1}	3.9023	–	4.0445	–	8
16	65	2.5073×10^{-1}	1.2684×10^{-1}	4.96	3.9144×10^{-1}	3.38	8
117	392	1.4004×10^{-1}	1.2284×10^{-2}	4.01	7.7812×10^{-2}	2.77	8
513	1620	7.0207×10^{-2}	1.0342×10^{-3}	3.58	1.9089×10^{-2}	2.04	8
12832	38897	1.7338×10^{-2}	1.1343×10^{-5}	3.23	1.0543×10^{-3}	2.07	8

The convergence behavior recalculated on the flat reference plate is summarized in Figure 6. As the maximum element size decreases from $h = 5.00 \times 10^{-1}$ to 1.73×10^{-2}, the relative L^2 error decreases monotonically from 3.90 to 1.13×10^{-5} and the relative H^1 error decreases from 4.04 to 1.05×10^{-3}. The two coarsest meshes are pre-asymptotic. A least-squares fit over the three finest meshes gives $\lVert e\rVert_{L^2}^{rel} = O(h^{3.33})$ and $\lVert e\rVert_{H^1}^{rel} = O(h^{2.06})$, in agreement with the $O(h^3)$ and $O(h^2)$ reference rates for a quadratic finite element. The former attribution of a reduced L^2 rate to the nonlinear Stefan–Boltzmann term and to the localized source has therefore been removed.

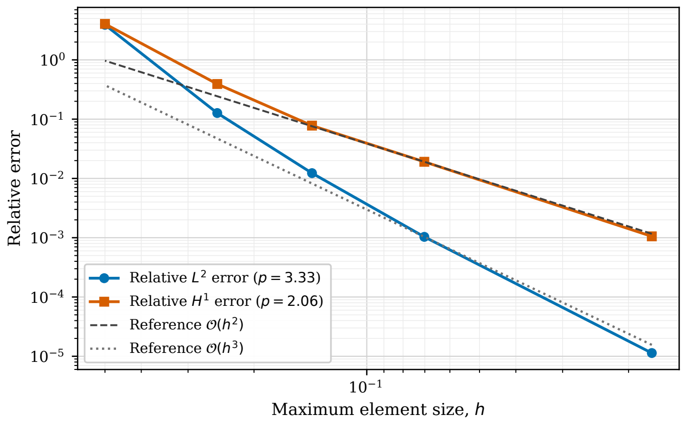

Figure 6. Convergence of the relative L^2 and H^1 error norms for the flat-plate MMS test as a function of the maximum element size h on a log–log scale. The norms are integrated directly against the exact manufactured field with the same 3×3 Gauss rule used in the finite element assembly. Reference slopes $O(h^2)$ and $O(h^3)$ are shown for comparison. Least-squares fits over the three finest meshes give $p = 2.06$ in H^1 and $p = 3.33$ in L^2.

5. Results

The representative parameters and computational settings used in the simulations are summarized in Table 2. The problem is governed by the two lumped constants $A = \varepsilon\sigma/(\delta k)$ and $B = \sigma T_S^4 H^2 R^2/(2\delta k)$, together with the plate dimensions and the source height H.

Table 2. Representative material properties and computational parameters used in the simulations. The constant B depends on the source height; with the values above it equals 1.16, 29.0, 116, and 1.16×10^4 for $H = 0.1$, 0.5, 1.0, and 10, respectively.

Parameter / setting	**Value**
Finite element type	Quad8 (bi-quadratic quadrilateral)
Mesh	structured quadrilateral grid ($n = 100$ edge subdivisions)
Newton relative tolerances (increment/residual)	$10^{-6}/10^{-6}$
Initial guess $T^{(0)}$	300 K
Plate dimensions $L_X \times L_Y$	1.0×1.0 m
Source horizontal position $(\bar{a}, \bar{b})$	plate center (0.5, 0.5)
Source heights H	0.1, 0.5, 1.0, 10.0 m
Stefan–Boltzmann constant σ	5.67×10^{-8} W m^{-2} K^{-4}
Thermal conductivity k	1.0 W m^{-1} K^{-1}
Emissivity ε	0.9
Plate thickness parameter δ	0.01 m
Source temperature T_S	800 K
Source radius R	0.01 m
Lumped constant $A = \varepsilon\sigma/(\delta k)$	5.10×10^{-6}
Lumped constant $B = \sigma T_S^4 R^2 H^2/(2\delta k)$	$1.161 \times 10^2 H^2$

5.1. Independent benchmark and physical mesh independence

Two complementary tests were conducted beyond the MMS verification. First, the spatially varying incident source was replaced by its uniform far-field value while retaining the nonlinear radiative loss and the homogeneous Neumann conditions. The resulting constant balance gives the reference temperature $T_{\text{ref}} = 21.84096$ K. Because a constant field is represented exactly by the Quad8 approximation, this test is expected to reach roundoff accuracy on every mesh; it checks the nonlinear source–loss balance, quadrature, and Newton linearization rather than a spatial convergence rate. Table 3 confirms this behavior: the relative L^2 and L^∞ errors remain between 2.0×10^{-14} and 1.6×10^{-12}.

Table 3. Uniform-irradiation benchmark with $T_{\text{ref}} = 21.84096$ K. The relative amplitude is $(T_{\max} - T_{\min})/T_{\text{ref}}$.

n	N_{el}	N_{dof}	$\lVert e\rVert_{L^2}^{rel}$	$\lVert e\rVert_{L^\infty}^{rel}$	Relative amplitude
10	117	392	1.998×10^{-14}	2.619×10^{-14}	1.334×10^{-14}
40	2054	6323	3.212×10^{-14}	6.019×10^{-14}	8.637×10^{-14}
100	12832	38897	1.573×10^{-12}	1.626×10^{-12}	1.148×10^{-13}

A separate mesh-independence study was then performed for the nonuniform physical source on the flat plate at $H = 0.1$, which is the case with the sharpest temperature gradient. All other parameters are those listed in Table 2; the 3×3 Gauss rule and the two relative Newton tolerances of 10^{-6} were retained. The area-weighted mean temperature was evaluated with the consistent mass matrix. For the profile comparison, the nodal solutions were linearly interpolated onto a common set of 2001 points along $x = y$, and E_{diag} denotes the relative L^2 difference from the refined $n = 160$ profile. All meshes converged in nine Newton updates.

Table 4. Physical mesh-independence study for the localized source on the flat plate at $H = 0.1$. Temperatures are given in K, and E_{diag} is reported as a percentage.

n	N_{el}	N_{dof}	h	$T_{\min}$	$T_{\max}$	T_{mean}	E_{diag} (%)
10	117	392	1.4004×10^{-1}	78.08749	134.84999	88.72543	8.464×10^{-1}
20	513	1620	7.0207×10^{-2}	78.17535	136.05446	88.86496	2.206×10^{-1}
40	2054	6323	3.7285×10^{-2}	78.17217	136.13966	88.85591	5.753×10^{-2}
80	8149	24768	2.0186×10^{-2}	78.17195	136.26257	88.85526	8.773×10^{-3}
100	12832	38897	1.7338×10^{-2}	78.17201	136.26108	88.85533	5.110×10^{-3}
160	32775	98966	1.0845×10^{-2}	78.17203	136.27229	88.85534	–

Between the production mesh ($n = 100$) and the refined reference ($n = 160$), the relative changes in $T_{\min}$, $T_{\max}$, and T_{mean} are $2.49 \times 10^{-5}\%$, $8.23 \times 10^{-3}\%$, and $1.98 \times 10^{-5}\%$, respectively, while the diagonal-profile difference is $5.11 \times 10^{-3}\%$. These results show that the $n = 100$ mesh used for the reported physical simulations is mesh independent to well below 0.01% for the monitored quantities.

Representative numerical results satisfy the analytical upper and lower bounds derived in Eqs (2.24) and (2.28) for all values of H considered in this study, as shown in Table 5. The values reported in this table are used to assess the consistency between the analytical estimates and the computed temperature range.

Table 5. Analytical upper and lower bounds, Eqs (2.24) and (2.28), compared with representative maximum and minimum temperatures observed in the simulations for the parameters of Table 2 (temperatures in K). The observed values lie within the bounds for every source height.

Height H	**Upper Bound**	**Lower Bound**	**Observed Max**	**Observed Min**
0.1	218.4	15.4	136.26	78.17
0.5	97.7	32.6	83.84	75.99
1.0	69.1	39.9	64.99	63.67
10.0	21.84	21.63	21.8229	21.8227

It is noteworthy that all simulated temperatures remain within the corresponding theoretical bounds. This agreement provides additional support for the mathematical consistency of the model and for the reliability of the numerical implementation.

It is also important to examine how the temperature field changes with the source height H, which represents the distance between the radiant source and the plate. The temperature distributions obtained for different values of H are shown in Figures 7a–8b.

Figures 7a and 7b show the temperature distributions for $H = 0.1$ and $H = 0.5$, respectively.

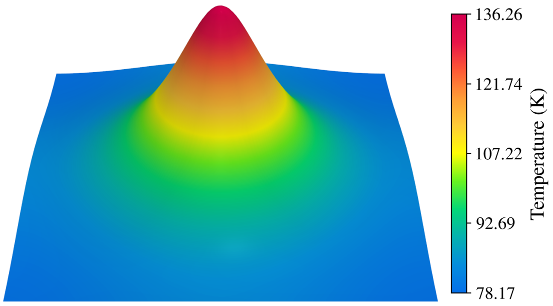

(a) Temperature distribution on plate with $H = 0.1$.

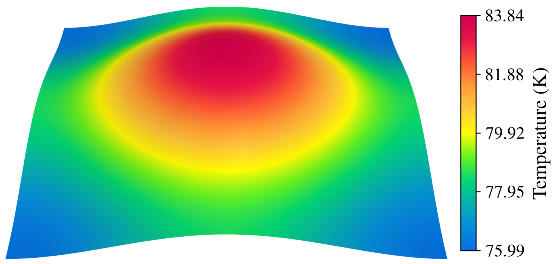

(b) Temperature distribution on plate with $H = 0.5$.

Figure 7. Temperature distribution on flat plates with $H = 0.1$ and $H = 0.5$.

In both cases, the source primarily affects the region located directly beneath it, producing a temperature peak centered near the plate axis. For $H = 0.1$, the thermal field is highly localized, with a sharp temperature gradient and a rapid decay away from the source projection. This behavior indicates that the radiative forcing is strongly concentrated in a small region of the plate. In contrast, for $H = 0.5$, the temperature profile becomes smoother and more spatially distributed, indicating that the incident radiative energy is less concentrated and that conduction within the plate plays a more visible role in redistributing heat.

Therefore, as H increases from 0.1 to 0.5, the maximum temperature decreases and the temperature gradient becomes less steep. This behavior is physically expected, since increasing the distance between the source and the plate reduces the concentration of radiative energy received at the central region.

Table 6. Comparison between temperature distributions for $H = 0.1$ and $H = 0.5$.

Feature	$H = 0.1$	$H = 0.5$
Maximum Temperature (K)	$\sim$ 140 (strong heating)	$\sim$ 84 (weaker heating)
Peak Sharpness	Very sharp and steep	Broader and smoother
Gradient	Steep drop from center to edges	Gentle gradient across surface
Heat Concentration	Highly localized	More distributed

Figures 8a and 8b show the temperature distributions for $H = 1.0$ and $H = 10.0$, respectively. For $H = 1.0$, a central temperature peak is still present, although it is significantly smoother and less intense than in the previous cases. This indicates that the source still has a noticeable thermal influence on the plate, but its effect is now spread over a wider region. For $H = 10.0$, the temperature field becomes nearly uniform, with a negligible difference between the maximum and minimum temperatures. This behavior reflects the progressive reduction of the radiative effect as the source is moved farther from the plate, since the corresponding view factor becomes very small.

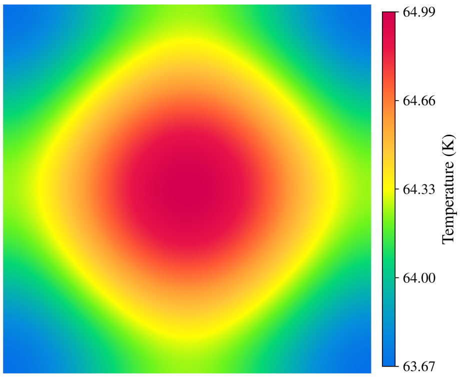

(a) Temperature distribution on plate with H = 1.0.

(b) Temperature distribution on plate with H = 10.0.

Figure 8. Temperature distribution on flat plates with H = 1.0 and H = 10.0.

Table 7. Comparison of temperature distributions for H = 1.0 and H = 10.0.

Feature	H = 1.0	H = 10.0
Maximum Temperature (K)	~ 65	~ 22
Peak Shape	Rounded and elevated	Almost flat
Gradient	Gradual slope from center	Nearly uniform surface
Heat Distribution	Mildly centralized	Uniform, very weak heating

Figure 9 compares the temperature profiles along the diagonal of the plate for different values of H. The numerical results are fully consistent with the expected physical behavior: smaller values of H produce sharper and more localized thermal peaks, whereas larger values of H lead to smoother and less pronounced temperature variations.

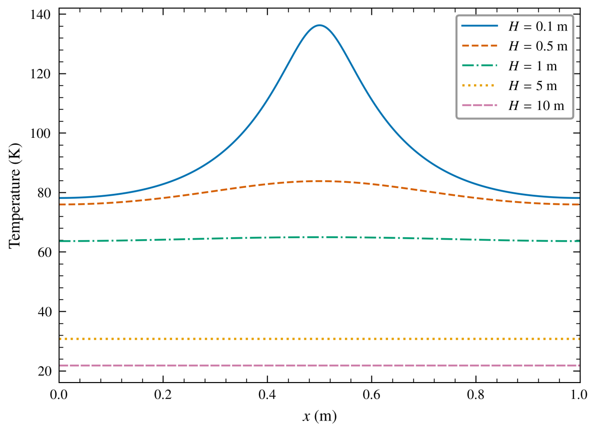

Figure 9. Comparative temperature distribution on flat plates.

Beyond this qualitative trend, the results quantify how strongly the source height controls the heating. The maximum temperature drops from 136.26 K at H = 0.1 to 83.84, 64.99, and 21.8229 K at H = 0.5, 1.0, and 10, respectively, corresponding to a reduction of approximately 84% over the range considered. At the same time, the difference between the maximum and minimum temperatures, which measures the in-plane non-uniformity, decreases from 58.09 K at $H = 0.1$ to less than 0.001 K at $H = 10$. At this largest height, the forcing itself becomes nearly spatially uniform since H greatly exceeds the plate dimensions, so both the reduced forcing gradient and conduction contribute to the near-uniform temperature field observed. The practical implication is that the controlling design parameter is not the source intensity alone but the source-to-plate distance, which simultaneously sets both the magnitude and the spatial spread of the thermal load.

The same surface formulation can also be applied, without modification, to non-flat meshes. In Figures 10a–11b, a corrugated sinusoidal surface with very low amplitude is considered, and the corresponding temperature fields are computed for the same values of H. The obtained profiles are qualitatively similar to those of the flat plate: for small source heights, the temperature distribution is strongly localized near the source projection, whereas for larger values of H, the thermal field becomes smoother and more diffuse. These examples are presented as a demonstration of the surface, or Laplace–Beltrami, finite element formulation on curved meshes, rather than as a rigorous treatment of curved-surface radiative exchange. Such a treatment would require a dedicated derivation of the incident-radiation term and the local view factor on a general curved geometry. In the present corrugated examples, radiative exchange between different regions of the same surface is neglected, which is consistent only with the very low-amplitude interpretation adopted here.

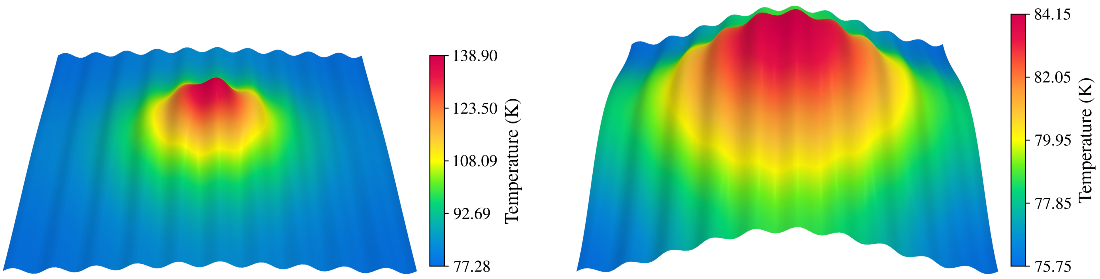

(a) Temperature distribution on corrugated plate with $H = 0.1$.

(b) Temperature distribution on corrugated plate with $H = 0.5$.

Figure 10. Temperature distribution on corrugated plates with $H = 0.1$ and $H = 0.5$.

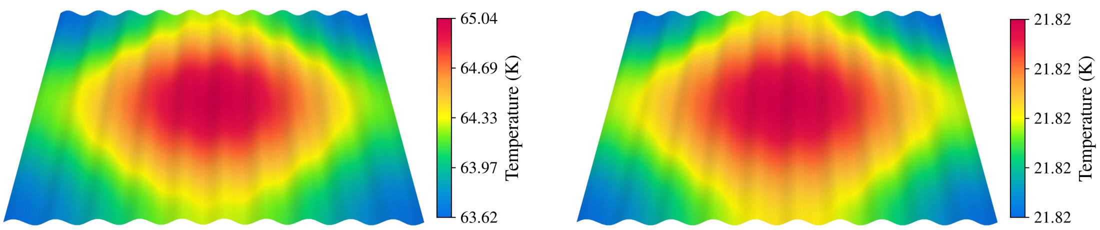

(a) Temperature distribution on corrugated plate with $H = 1.0$.

(b) Temperature distribution on corrugated plate with $H = 10.0$.

Figure 11. Temperature distribution on corrugated plates with $H = 1.0$ and $H = 10.0$.

Because the formulation is assembled element by element on the surface mesh, geometric discontinuities such as holes are handled directly, without any change to the discrete finite element structure: the hole is represented by the absence of elements, and the homogeneous Neumann condition applies naturally along the resulting internal edge. Figures 12a and 12b show representative simulations for this configuration, which are again reported as demonstrations of the meshing capability rather than as a separate physical model.

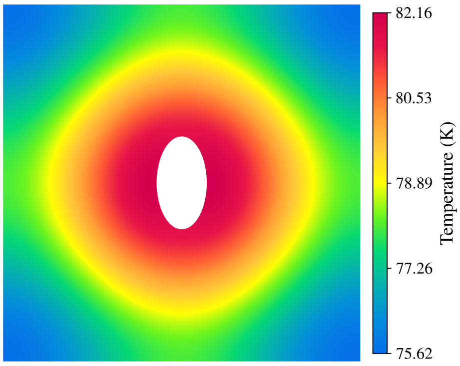

(a) Temperature distribution on flat plate with hole.

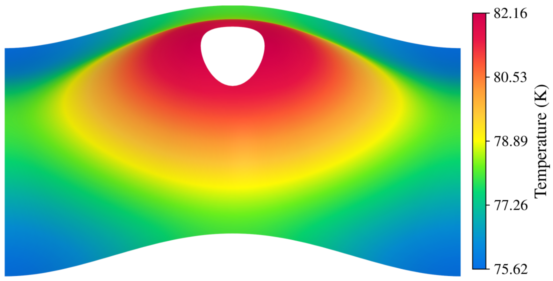

(b) Temperature distribution on flat plate with hole, warped view.

Figure 12. Temperature distribution on flat plate with hole, two views.

6. Conclusions

This study developed a combined analytical and numerical framework for predicting the steady-state temperature field induced on a thin plate by a small, localized radiative source placed at a finite distance. The model couples in-plane conduction with two-sided nonlinear radiative losses and a view-factor-based source term, under homogeneous Neumann boundary conditions, yielding a nonlinear boundary-value problem governed by the Stefan–Boltzmann law. The problem was solved by a Newton-linearized weak formulation discretized with Quad8 finite elements, and the implementation was verified with the method of manufactured solutions, for which both the relative L^2 and H^1 errors decreased monotonically under mesh refinement.

Explicit a priori upper and lower bounds were derived, and, for all source heights examined, the computed temperatures remained within these bounds. The source height was found to be the dominant parameter: as H increased from 0.1 to 10, the peak temperature decreased from about 140 to about 22 K, corresponding to a reduction of roughly 84%, and the in-plane temperature difference collapsed from about 62 K to less than 0.01 K, the field becoming essentially uniform as conduction redistributed the absorbed energy. The same surface formulation was also applied, as a demonstration, to a very low-amplitude corrugated plate and to a plate with a hole, producing qualitatively consistent fields.

The present results were obtained under the assumptions of an opaque gray plate with full absorption of the incident flux, a thin-plate membrane conduction model, and a small disk-like source. Within this scope, the framework provides a consistent approach to nonlinear radiative–conductive heat transfer driven by a distant source. From a practical standpoint, the framework is directly relevant to infrared-lamp and radiant-panel heating of plates and moving webs, radiant testing of surfaces, and the thermal design of components placed near concentrated high-temperature sources, for which the source-to-plate distance H, identified here as the dominant parameter, provides a direct design lever for controlling both the peak temperature and its spatial uniformity. Natural extensions include a rigorous formulation of the incident-radiation term on general curved surfaces, the treatment of partially reflecting and non-gray surfaces, multiple or extended sources, and validation against independent benchmark or experimental data.

Appendix A. Newton linearized system

We start from the nonlinear variational problem:

$$
\begin{aligned}
F(T;v) = &\oint_{\partial\Omega} v(k\nabla T)\cdot \mathbf{n}\, dS - \int_{\Omega} (k\nabla T)\cdot \nabla v\, d\Omega \\
&- k\int_{\Omega} A|T|^3 T v\, d\Omega + k\int_{\Omega} \frac{B}{[(\bar{a}-x)^2 + (\bar{b}-y)^2 + H^2]^2} v\, d\Omega = 0.
\end{aligned} \tag{A.1}
$$

At iteration n, we linearize F around $T^{(n)}$ and solve for $\Delta T = T^{(n+1)} - T^{(n)} \in V$ such that:

$$
-DF(T^{(n)};\Delta T, v) = F(T^{(n)}; v). \tag{A.2}
$$

The Gâteaux derivative $DF(T^{(n)};\Delta T, v)$ reads:

$$
DF(T^{(n)};\Delta T, v) = \oint_{\partial\Omega} v(k\nabla \Delta T)\cdot \mathbf{n}\, dS - \int_{\Omega} (k\nabla \Delta T)\cdot \nabla v\, d\Omega - \int_{\Omega} 4kA|T^{(n)}|^3 \Delta T v\, d\Omega. \tag{A.3}
$$

The extension $|T|^3 T$ (rather than T^4) is used because it remains a well-defined, smooth, monotone function on all of $\mathbb{R}$, so the Newton iteration above stays well-posed even if an intermediate iterate were to become negative. The a priori lower bound derived in Section 2 is strictly positive for every source height considered and applies to the converged weak solution; since the finite element solution converges to this solution under mesh refinement (Section 4) and every observed minimum lies above the corresponding analytical lower bound, the converged numerical temperature field is positive in all cases reported. This guarantees positivity of the converged solution rather than of every intermediate Newton iterate; no formal positivity-preservation result is claimed for the iteration itself.

Under Dirichlet boundary conditions, the test function v vanishes on Γ_D where T is prescribed, so the corresponding boundary integral vanishes there for that reason; under homogeneous Neumann conditions on the remainder of the boundary (or on the entire boundary, for the physical problem), the flux term vanishes directly from the boundary condition $\nabla T \cdot \mathbf{n} = 0$. Both boundary integrals therefore vanish, but for different reasons depending on the boundary type. For nonhomogeneous Neumann conditions, both integrals remain and must be evaluated using the definition of boundary elements for the integrals on $\partial\Omega$. Therefore, the linearized weak form becomes the following: Find $\Delta T \in V$ such that

$$
-\oint_{\partial\Omega} v(k\nabla \Delta T)\cdot \mathbf{n}\, dS + \int_{\Omega} (k\nabla \Delta T)\cdot \nabla v\, d\Omega + \int_{\Omega} 4kA|T^{(n)}|^3 \Delta T v\, d\Omega = F(T^{(n)}; v), \tag{A.4}
$$

and update:

$$
T^{(n+1)} = T^{(n)} + \Delta T. \tag{A.5}
$$

To solve the nonlinear radiative heat transfer problem, the Newton-Raphson algorithm is employed within the finite element framework. The procedure begins by expressing the nonlinear governing equation in its weak form, which is then discretized using a finite-dimensional subspace of basis functions. At each iteration, the current approximation of the temperature field is updated by solving a linear system derived from the Gâteaux derivative of the weak form, this yields the Jacobian matrix, and the associated residual vector. Specifically, the linear system $J(T^{(n)})\Delta T = -R(T^{(n)})$ is solved for the Newton increment ΔT, which is used to update the solution via $T^{(n+1)} = T^{(n)} + \Delta T$.

The convergence test is applied over the free degrees of freedom $\mathcal{F}$ using

$$\eta_T^{(n+1)} = \frac{\|\Delta T_{\mathcal{F}}^{(n+1)}\|_2}{\max\left(1, \|T_{\mathcal{F}}^{(n+1)}\|_2\right)}, \qquad \eta_R^{(n)} = \frac{\|\mathbf{R}_{\mathcal{F}}^{(n)}\|_2}{\max\left(1, \|\mathbf{R}_{\mathcal{F}}^{(0)}\|_2\right)}.$$

The iteration is accepted only when both indicators are below 10^{-6}.

The residual vector used in the implementation is written below. Let $T_h^{(n)} = \sum_j N_j T_j^{(n)}$ denote the finite element temperature evaluated pointwise on each Ω_e, and define the nodal source values $f_j = kB/[(\bar{a} - x_j)^2 + (\bar{b} - y_j)^2 + H^2]^2$.

$$\begin{aligned}\mathbf{R}_i^{(n)} = &-\sum_j \left[\int_\Omega (k\nabla_s N_i) \cdot \nabla_s N_j \, d\Omega\right] T_j^{(n)} - \sum_e \int_{\Omega_e} kA \left|T_h^{(n)}\right|^3 T_h^{(n)} N_i \, d\Omega \\ &+ \sum_j \left[\int_\Omega N_i N_j \, d\Omega\right] f_j.\end{aligned} \tag{A.6}$$

$$R_{i,\mathrm{cond}}^{(n)} = -\sum_j \left[\int_\Omega (k\nabla_s N_i) \cdot \nabla_s N_j \, d\Omega\right] T_j^{(n)}, \tag{A.7}$$

$$R_{i,\mathrm{rad}}^{(n)} = -\sum_e \int_{\Omega_e} kA \left|T_h^{(n)}\right|^3 T_h^{(n)} N_i \, d\Omega, \tag{A.8}$$

$$R_{i,\mathrm{src}} = \sum_j \left[\int_\Omega N_i N_j \, d\Omega\right] f_j. \tag{A.9}$$

Thus, the nonlinear radiative residual contains a single test function N_i; the product $N_i N_j$ arises after expanding $T_h^{(n)}$ and in the radiation Jacobian. Both $T_h^{(n)}$ and $4A|T_h^{(n)}|^3$ are evaluated at the quadrature points. In matrix notation, the implemented contribution is $-\mathbf{M}_{\mathrm{rad},s}^{(n)} T^{(n)}/4$. The last term also makes the source treatment explicit: the incident-radiation field is evaluated at the nodes and projected through the consistent mass matrix, $\sum_j M_{ij} f_j$, rather than evaluated by direct quadrature of the exact spatial source $f(x, y)$.

At each Newton iteration step n, the nonlinear weak form is linearized, resulting in a matrix system that relates the Newton increment $\Delta T^{(n+1)}$ to the residual evaluated at the current iterate $T^{(n)}$. This yields the following linear system:

$$\left[\mathbf{K_s} + \mathbf{M_{rad_s}}^{(n)}\right] \Delta T^{(n+1)} = -\left[\mathbf{K_s} + \frac{\mathbf{M_{rad_s}}^{(n)}}{4}\right] T^{(n)} + \mathbf{M_s f}. \tag{A.10}$$

$$T^{(n+1)} = T^{(n)} + \Delta T \tag{A.11}$$

where $\mathbf{K_s}$ is the general stiffness matrix corresponding to thermal diffusion for a two-dimensional surface embedded in $\mathbb{R}^3$, $\mathbf{M_{rad_s}}^{(n)}$ is the nonlinear radiation matrix evaluated at $T^{(n)}$, and the final term on the right-hand side represents the external radiative source projected onto the finite element space through the mass matrix $\mathbf{M_s}$. After solving this linear system, the temperature field is updated as $T^{(n+1)} = T^{(n)} + \Delta T^{(n+1)}$. The process is repeated until both relative criteria defined above are satisfied. No damping or line-search procedure is used in the reported calculations.

Author contributions

J. L. Silva Neto: Conceptualization, Methodology, Numerical Implementation, Investigation, Writing original draft; E. D. Correa: Conceptualization, Methodology, Supervision, Validation, Writing–review and editing; R. M. S. Gama: Conceptualization, Mathematical analysis, Supervision, Writing–review and editing; G. R. Anjos: Methodology, Numerical analysis, Visualization, Writing–review and editing. All authors have read and approved the final version of the manuscript.

Use of Generative-AI tools declaration

The authors declare that they have not used Artificial Intelligence (AI) tools in the creation of this article.

Acknowledgments

The research leading to these results received funding from the Conselho Nacional de Desenvolvimento Científico e Tecnológico (CNPq), and the Research Support Foundation of the State of Rio de Janeiro (FAPERJ).

Conflict of interest

All authors declare no conflicts of interest in this paper.

References

1. S. Chen, Q. Duan, Tangent stiffness for nonlinear heat transfer and its application to heterogeneous materials, *Int. J. Heat Mass Transfer*, **181** (2021), 121888. https://doi.org/10.1016/j.ijheatmasstransfer.2021.121888
2. K. H. Wu, C. Y. Wu, Transient two-dimensional radiative and conductive heat transfer in an axisymmetric medium, *Heat Mass Transfer*, **33** (1998), 327–331. https://doi.org/10.1007/s002310050197
3. J. Tencer, J. R. Howell, Coupling radiative heat transfer in participating media with other heat transfer modes, *J. Braz. Soc. Mech. Sci. Eng.*, **38** (2015), 1473–1487. https://doi.org/10.1007/s40430-015-0434-1
4. M. F. Modest, *Radiative Heat Transfer*, 3 Eds, New York: Academic Press, 2013.
5. R. Siegel, J. R. Howell, *Thermal Radiation Heat Transfer*, 4 Eds, Abingdon: Taylor & Francis, 2002.

6. H. Zhou, G. Qin, S. Jing, Heat transfer for nonlinear boundary conditions involving radiation for constant and temperature related thermal conductivity material using the mwls method, *Eng. Anal. Bound. Elem.*, **128** (2021), 290–297. https://doi.org/10.1016/j.enganabound.2021.04.013

7. Y. Filipov, I. Faragó, E. Avdzhieva, P. Filipov, A coupled pde–ode model for nonlinear transient heat transfer with convection heating at the boundary, *Axioms*, **12** (2023), 323. https://doi.org/10.3390/axioms12040323

8. S. Ouchtout, B. Rousseau, Y. Favennec, Finite element framework for modeling conducto-radiative transfers within heterogeneous media at both discrete and continuous scales, *Int. J. Heat Mass Transfer*, **197** (2022), 123274. https://doi.org/10.1016/j.ijheatmasstransfer.2022.123274

9. M. L. Martins-Costa, R. M. S. Gama, Temperature distribution in porous fins with radiation and temperature-dependent conductivity, *Revista Engenharia Térmica*, **19** (2020), 45–53.

10. M. K. Gupta, K. J. Bumtariya, H. Shukla, P. Patel, Z. Khan, Methods for evaluation of radiation view factor: A review, *Mater. Today Proc.*, **4** (2017), 1236–1243. https://doi.org/10.1016/j.matpr.2017.01.143

11. M. Singh, A discrete-ordinate weak galerkin method for radiative transfer equation, *Appl. Numer. Math.*, **201** (2024), 628–641. https://doi.org/10.1016/j.apnum.2024.02.009

12. D. Kitzmann, J. Bolte, A. B. C. Patzer, Discontinuous galerkin finite element methods for radiative transfer in spherical symmetry, *Astron. Astrophys.*, **595** (2016), A90. https://doi.org/10.1051/0004-6361/201628578

13. Y. Liu, X. Zhang, M. W. Lu, A meshless method based on least-squares approach for steady- and unsteady-state heat conduction problems, *Numer. Heat Transfer, Part B*, **47** (2005), 257–275. https://doi.org/10.1080/10407790590901648

14. A. S. Hashemi, M. Heydari, G. B. Loghmani, Iterative compact finite difference method for the numerical study of fully wet porous fins with different profile shapes, *Appl. Numer. Math.*, **186** (2023), 358–377. https://doi.org/10.1016/j.apnum.2023.01.021

15. W. Qu, H. He, A spatial–temporal gfdm with an additional condition for transient heat conduction analysis of fgms, *Appl. Math. Lett.*, **110** (2020), 106579. https://doi.org/10.1016/j.aml.2020.106579

16. X. Zheng, W. Qu, Y. Gu, A time spectral generalized finite difference method for three-dimensional transient heat conduction analysis in functionally graded materials with space–time coefficients, *Int. J. Numer. Meth. Eng.*, **127** (2026), e70259. https://doi.org/10.1002/nme.70259

17. L. M. Ruan, W. An, H. P. Tan, H. Qi, Least-squares finite-element method of multidimensional radiative heat transfer in absorbing and scattering media, *Numer. Heat Transfer, Part A*, **51** (2007), 657–677. https://doi.org/10.1080/10407780600939578

18. D. Büschgens, C. Steimer, H. Pitsch, Radiation modelling of arbitrary two-dimensional surfaces using the surface-to-surface approach extended with a blocking algorithm, *Heat Mass Transfer*, **58** (2022), 1637–1648. https://doi.org/10.1007/s00231-022-03203-4

19. V. Kumar, M. D. Alsulami, I. E. Sarris, B. C. Prasannakumara, S. Rana, Backpropagated neural network modeling for the non-fourier thermal analysis of a moving plate, *Mathematics*, **11** (2023), 438. https://doi.org/10.3390/math11020438

20. E. D. Correa, J. M. Quirino, R. L. Sobral, J. F. Corrêa, R. M. S. Gama, An analytical and a numerical method for nonlinear convection-radiation problems in porous fins, *Adv. Math. Phys.*, **2022** (2022), 9033324. https://doi.org/10.1155/2022/9033324

21. V. V. Sarmento, M. L. Martins-Costa, R. M. S. da Gama, A model for a set of porous fins on a long rotating cylinder considering thermal radiation and natural convection, *Numer. Heat Transfer, Part B*, **84** (2023), 234–252. https://doi.org/10.1080/10407790.2023.2200215

22. S. Kanwal, S. A. A. Shah, A. Bariq, B. Ali, A. E. Ragab, E. A. Az-Zo'bi, Insight into the dynamics of heat and mass transfer in nanofluid flow with linear/nonlinear mixed convection, thermal radiation, and activation energy effects over the rotating disk, *Sci. Rep.*, **13** (2023), 23031. https://doi.org/10.1038/s41598-023-49988-0

23. B. Ali, H. Sharif, D. Habib, H. A. Ghazwani, I. Saman, H. Yang, Significance of tri-hybrid nanoparticles in thermal management subject to magnetized squeezing flow of a boger-micropolar nanofluid between concentring disks, *J. Mol. Liq.*, **397** (2024), 124141. https://doi.org/10.1016/j.molliq.2024.124141

24. M. M. Bhatti, M. Marin, A. Öchsner, R. Ellahi, Parametric analysis of quadratic convection on granular material flow through an inclined heated plane with heat absorption/generation, *Continuum Mech. Thermodyn.*, **37** (2025), 87. https://doi.org/10.1007/s00161-025-01416-6

25. S. F. Ramadan, M. M. Bhatti, K. S. Mekheimer, A. M. A. S. Moawad, C. M. Khalique, Magneto-bioconvection dynamics of synovial nanofluids: Consequences of porosity, rheology, and heat generation, *J. Comput. Appl. Mech.*, **57** (2026), 122–133. https://doi.org/10.22059/jcamech.2025.406289.1690

26. B. Vujanovic, A. M. Strauss, Heat transfer with nonlinear boundary conditions via a variational principle, *AIAA J.*, **9** (1971), 327–339. https://doi.org/10.2514/3.6173

27. M. T. Darvishi, R. S. R. Gorla, F. Khani, B. J. Gireesha, Thermal analysis of natural convection and radiation in a fully wet porous fin, *Int. J. Numer. Meth. Heat Fluid Flow*, **26** (2016), 2419–2431. https://doi.org/10.1108/HFF-06-2015-0230

28. B. K. Jha, G. Samaila, Thermal radiation effect on boundary layer over a flat plate having convective surface boundary condition, *SN Appl. Sci.*, **2** (2020), 381. https://doi.org/10.1007/s42452-020-2167-8

29. K. Chandan, K. Karthik, K. V. Nagaraja, B. C. Prasannakumara, R. S. Varun Kumar, T. Muhammad, Radiative heat transfer analysis of a concave porous fin under the local thermal non-equilibrium condition, *Appl. Math. Mech.-Engl. Ed.*, **45** (2024), 1613–1632. https://doi.org/10.1007/s10483-024-3143-6

30. G. Sowmya, M. M. A. Lashin, M. Ijaz Khan, R. S. Varun Kumar, K. C. Jagadeesha, B. C. Prasannakumara, et al., Significance of convection and internal heat generation on the thermal distribution of a porous dovetail fin with radiative heat transfer, *Micromachines*, **13** (2022), 1336. https://doi.org/10.3390/mi13081336

31. M. R. Nigri, J. J. Pedrosa-Filho, R. M. S. Gama, An exact solution for the heat transfer process in infinite cylindrical fins with any temperature-dependent thermal conductivity, *Thermal Sci. Eng. Prog.*, **32** (2022), 101333. https://doi.org/10.1016/j.tsep.2022.101333

32. C. J. Permann, D. R. Gaston, D. Andrs, R. W. Carlsen, F. Kong, A. D. Lindsay, et al., Moose: Enabling massively parallel multiphysics simulation, *SoftwareX*, **11** (2020), 100430. https://doi.org/10.1016/j.softx.2020.100430

33. G. Dziuk, C. M. Elliott, Finite element methods for surface pdes, *Acta Numer.*, **22** (2013), 289–396. https://doi.org/10.1017/S0962492913000056

34. M. A. Olshanskii, A. Reusken, Trace finite element methods for pdes on surfaces, In: *Geometrically Unfitted Finite Element Methods and Applications*, Berlin: Springer, 2017, 211–258. https://doi.org/10.1007/978-3-319-71431-8_7

35. R. Adams, J. Fournier, *Sobolev Spaces*, Amsterdam: Elsevier, 2003.

AIMS Press